J𝕄 PAPERS

Heat transport and temperature boundary-layer profiles in closed turbulent Rayleigh–Bénard convection with slippery conducting surfaces

Maojing Huang[1], **Yin Wang**[2,3], **Yun Bao**[4] and **Xiaozhou He**[1,5],†

[1]School of Mechanical Engineering and Automation, Harbin Institute of Technology, Shenzhen 518055, China

[2]Department of Physics, Hong Kong University of Science and Technology, Clear Water Bay, Kowloon, Hong Kong, China

[3]Princeton Plasma Physics Laboratory, Princeton University, Princeton, NJ 08543, USA

[4]Department of Mechanics, Sun Yat-Sen University, Guangzhou 510275, China

[5]Max Planck Institute for Dynamics and Self-Organization, Am Fassberg 17, 37077 Göttingen, Germany

We report direct numerical simulations (DNS) of the Nusselt number Nu, the vertical profiles of mean temperature $\Theta(z)$ and temperature variance $\Omega(z)$ across the thermal boundary layer (BL) in closed turbulent Rayleigh–Bénard convection (RBC) with slippery conducting surfaces (z is the vertical distance from the bottom surface). The DNS study was conducted in three RBC samples: a three-dimensional cuboid with length $L = H$ and width $W = H/4$ (H is the sample height), and two-dimensional rectangles with aspect ratios $\Gamma \equiv L/H = 1$ and 10. The slip length b for top and bottom plates varied from 0 to ∞. The Rayleigh numbers Ra were in the range $10^6 \leqslant Ra \leqslant 10^{10}$ and the Prandtl number Pr was fixed at 4.3. As b increases, the normalised Nu/Nu_0 (Nu_0 is the global heat transport for $b = 0$) from the three samples for different Ra and Γ can be well described by the same function $Nu/Nu_0 = N_0 \tanh(b/\lambda_0) + 1$, with $N_0 = 0.8 \pm 0.03$. Here $\lambda_0 \equiv L/(2Nu_0)$ is the thermal boundary layer thickness for $b = 0$. Considering the BL fluctuations for $Pr > 1$, one can derive solutions of temperature profiles $\Theta(z)$ and $\Omega(z)$ near the thermal BL for $b \geqslant 0$. When $b = 0$, the solutions are equivalent to those reported by Shishkina *et al.* (*Phys. Rev. Lett.*, vol. 114, 2015, 114302) and Wang *et al.* (*Phys. Rev. Fluids*, vol. 1, 2016, 082301(R)), respectively, for no-slip plates. For $b > 0$, the derived solutions are in excellent agreement with our DNS data for slippery plates.

Key words: boundary layer structure, Bénard convection

† Email address for correspondence: hexiaozhou@hit.edu.cn

M. Huang, Y. Wang, Y. Bao and X. He

1. Introduction

Turbulent thermal convection with slippery surfaces is typically considered as the predominant process of heat transport in many natural systems, for instance the oceans (Davis 1991), the Earth's mantle (Moore & Webb 2013) and the atmosphere of Venus (Tritton 1975), where heat exchanges are applied on fluid–fluid interfaces. Such convection also plays an important role in heat transport in numerous technical applications using either superhydrophobic surfaces (Choi & Kim 2006), internal heating (Wang, Lohse & Shishkina 2021) or injecting elastic additives – such as polymers (White & Mungal 2008) or bubbles (Ceccio 2010) – to reduce the resistance on solid–fluid interfaces. In these cases, the slippage can be characterised by the slip length b, which connects the velocity u_s and stress $(\partial u/\partial n)_s$ on the surface via $u_s = b(\partial u/\partial n)_s$. On a no-slip (NS) surface, the velocity $u = 0$ leads to the slip length $b = 0$; while on a free-slip (FS) surface, the stress $\partial u/\partial n = 0$, resulting in $b \to \infty$. In the practical flows of interest, the slip length b is often assumed to be a finite constant.

Convection flow is often considered in a layer of viscous fluid heated from below and cooled from above, which is known as Rayleigh–Bénard convection (RBC) (Ahlers 2009; Ahlers, Grossmann & Lohse 2009; Lohse & Xia 2010). Its properties are characterised by the Rayleigh number $Ra \equiv \alpha g \Delta H^3/(\kappa \nu)$, the Prandtl number $Pr \equiv \nu/\kappa$ and the geometry of the convection sample. Here g is the gravitational acceleration; $\Delta = T_b - T_t$ is the temperature difference between the lower (T_b) and upper (T_t) horizontal plates separated by distance H; and α, κ and ν are, respectively, the thermal expansion coefficient, the thermal diffusivity and the kinematic viscosity of the fluid. The RBC global heat transport is expressed in the dimensionless form, known as the Nusselt number, $Nu \equiv jH/(k\Delta)$, with j the heat flux and k the fluid thermal conductivity.

Recent direct numerical simulation (DNS) studies have shown that a slippery surface has complex effects on turbulent heat transport in RBC. With horizontally periodic boundary conditions, the convection flow was found to form into different patterns, zonal flow or large-scale circulation (LSC), depending on initial conditions and Ra (Goluskin *et al.* 2014; Wang *et al.* 2020*a*; Huang & He 2022). For zonal flow, Nu for free-slip plates is ∼80 % lower than that for no-slip plates (Goluskin *et al.* 2014; van der Poel *et al.* 2014; Von Hardenberg *et al.* 2015); while for LSC, the free-slip Nu is ∼80 % higher (Huang & He 2022). In a closed RBC sample, Nu increases by ∼7 % when the sidewalls are free-slip but the horizontal plates are no-slip (Kaczorowski, Chong & Xia 2014). For all free-slip boundaries, the increment is above 80 % compared with all no-slip boundaries (Pandey & Verma 2016). In free thermal convection over a horizontal heated plate, heat transport across a free-slip surface is 60 % higher than across a no-slip surface (Mellado 2012). With different Pr and sample geometries, the efficiencies of heat transport in RBC with slippery surfaces are found to vary in a wide range (Goluskin 2015; Wang *et al.* 2020*a,b*; Wen *et al.* 2020).

Since convective heat transport is mainly determined by the structure and fluctuations of the boundary layer (BL) in RBC (Shishkina, Weiss & Bodenschatz 2016; Weiss *et al.* 2018), the study of temperature BL profiles is vital for a better understanding of the underlying mechanism. When Ra is relatively low, the BL is laminar and the mean temperature BL profiles can be well described by the laminar Prandtl BL equations with appropriate boundary conditions (Schlichting & Gersten 2000). In this case, Nu follows the classical scaling $Nu \sim Ra^{\gamma_c}$, with the effective exponent γ_c varying from 0.28 for Ra near 10^8 to 0.32 for Ra near 10^{11} (see e.g. Ahlers *et al.* 2012*b*). When Ra is sufficiently

high, on the other hand, the BL is expected to be fully turbulent due to strong shear by the turbulent interior flow. In this case, the temperature BL structure is predicted to follow a logarithmic spatial variation near the boundaries (Kraichnan 1962; Spiegel 1971; Shraiman & Siggia 1990; Grossmann & Lohse 2011), which has been observed in both experiments (Ahlers *et al.* 2012*a*; Ahlers, Bodenschatz & He 2014; He, Bodenschatz & Ahlers 2021*b*) and DNS (van der Poel *et al.* 2015). Accordingly, *Nu* is predicted to follow the ultimate scaling $Nu \sim Ra^{\gamma_u}$ with effective exponent $\gamma_u = 0.5$ plus an *Ra*-dependent log correction (Grossmann & Lohse 2000, 2001, 2011; Stevens *et al.* 2013) that comes from the effects of the no-slip solid walls. When the aspect ratio Γ – the ratio of the sample lateral extension to its height – is close to one, it is found that $Nu \sim Ra^{\gamma_{eff}}$, with the 'local' scaling exponent $\gamma_{eff} \simeq 0.38$ for the transition Rayleigh number $Ra^* \simeq 10^{14}$ (Ahlers *et al.* 2012*b*; He *et al.* 2012*a*,*b*, 2021*b*), which agrees well with the prediction for the ultimate state by Grossmann & Lohse (2011). More experimental evidence has revealed that the local slope γ_{eff} increases as *Ra* increases (He, Bodenschatz & Ahlers 2020*a*) and Ra^* increases as Γ decreases (He, Bodenschatz & Ahlers 2020*b*). For a slender sample with an aspect ratio of 1/10, it is found in DNS that the classical scaling $Nu \sim Ra^{1/3}$ can hold up to $Ra = 10^{15}$ (Iyer *et al.* 2020). For details about the aspect-ratio effects on the ultimate-state transition, please see the review by Ahlers *et al.* (2022) and references therein.

In recent years, significant advances have been made for the equations of the temperature BL profiles for a moderate *Ra* between the above two extreme cases, which is related to a class of practical convection flows. By considering turbulent viscosity and diffusivity, equations of the mean temperature BL profiles were derived for different *Pr* (Shishkina *et al.* 2015, 2017; Ching, Dung & Shishkina 2017; Ching *et al.* 2019). Equations of the temperature variance profiles for different *Pr* were derived near the thermal BL (Wang, He & Tong 2016; Xu *et al.* 2021), in the mixing zone (Wang *et al.* 2018) and in the log layer (He, Bodenschatz & Ahlers 2021*a*; He *et al.* 2021*b*). In horizontal convection, where the flow is asymmetric, equations of the mean temperature profiles were derived near the hot and cold BLs, respectively, based on the LSC structure of the fluid (Yan, Shishkina & He 2021). The predicted temperature equations have been extensively tested in experiments and DNS over a wide range of parameters for no-slip surfaces. With different boundary conditions, the slippery plates also affect the temperature profiles near the thermal BL in RBC. It still remains unclear, however, what the equations of temperature BL profiles for slippery RBC are and how the corresponding heat transport efficiency changes with the slip length.

In this paper, we explore in DNS the global heat transport and the temperature BL profiles in closed turbulent RBC samples with no-slip sidewalls and slippery horizontal plates that have a varying slip length $b > 0$. Many, if not most, of the studies in RBC have focused on two ideal boundary conditions: no-slip and free-slip. That leaves a broad parameter range in between for the studies on solid boundaries of varying slip length. That is a primary motivation in this work. We conducted DNS in two- and three-dimensional (2-D and 3-D) RBC samples of three different aspect ratios in the range $10^6 \leqslant Ra \leqslant 10^{10}$ with $Pr = 4.3$ (water). From the DNS, we found the normalised heat transport $Nu(b)/Nu_0$ for different *b* and *Ra* can be overlapped onto a single master curve, once the slip length *b* is normalised by the no-slip thermal BL thickness λ_0. The overlapped curve can be well described by the function $Nu/Nu_0 = N_0 \tanh(b/\lambda_0) + 1$, with $N_0 = 0.8 \pm 0.03$. To the best of our knowledge, this scaling function is obtained in RBC for the first time. Similar to the ideas of Shishkina *et al.* (2015) and Wang *et al.* (2016), we derived

general equations for the profiles of both the mean temperature and temperature variance near a slippery plate. These equations were thoroughly tested in 2-D and 3-D samples in the studied range of *Ra* and *b*. Our data revealed that, for a fixed *Pr*, the equation parameters depend only on *b*. For $b = 0$, these temperature equations are the same as those derived by Shishkina *et al.* (2015) and Wang *et al.* (2016) for no-slip plates. For $b > 0$, the general equations are expected to apply to a class of convection flows with slippery horizontal plates, ranging from many natural processes to numerous engineering systems.

The rest of this paper is organised as follows. We first explain the method and parameters that were used in the DNS of RBC with slippery conducting plates in § 2. Then, § 3 presents the results of the global heat transport *Nu* for a varying slip length $b \geqslant 0$. In § 4 we first derive general equations for the mean temperature and temperature variance profiles near the BL in slippery RBC. Then we show good agreement between the DNS data and the predicted temperature profiles for varying $b \geqslant 0$. Finally, a brief summary is given in § 5.

2. Direct numerical simulation

With the Oberbeck–Boussinesq approximation, the dimensionless governing equations for incompressible turbulent RBC flow are

$$\hat{\nabla} \cdot \hat{\boldsymbol{u}} = 0, \tag{2.1}$$

$$\partial_{\hat{t}} \hat{\boldsymbol{u}} + (\hat{\boldsymbol{u}} \cdot \hat{\nabla}) \hat{\boldsymbol{u}} = -\hat{\nabla} \hat{p} + \frac{1}{\sqrt{Ra/Pr}} \hat{\nabla}^2 \hat{\boldsymbol{u}} + \hat{\theta} \boldsymbol{e}_{\hat{z}}, \tag{2.2}$$

$$\partial_{\hat{t}} \hat{\theta} + (\hat{\boldsymbol{u}} \cdot \hat{\nabla}) \hat{\theta} = \frac{1}{\sqrt{Ra\,Pr}} \hat{\nabla}^2 \hat{\theta}. \tag{2.3}$$

The dimensionless fields of velocity $\hat{\boldsymbol{u}}$, temperature $\hat{\theta}$ and pressure $\hat{p}$, as well as length and time, are in the units of the free-fall velocity $U_f = \sqrt{\alpha g H \Delta}$, the applied temperature difference Δ, the free-fall pressure $p_f = \rho \alpha g H \Delta$, the sample height H and the free-fall time $T_f = \sqrt{H/(\alpha g \Delta)}$, respectively.

We used a finite-difference code to solve the above governing equations. The DNS code has been used and described in detail in previous studies (Bao *et al.* 2015; Chen *et al.* 2017; Zhang *et al.* 2018). Here we only mention some of the key information. The Rayleigh numbers were in the range $10^6 \leqslant Ra \leqslant 10^{10}$ and the Prandtl number $Pr = 4.3$. The DNS were performed in three RBC samples of different geometries. One of them was a 3-D cuboid, as shown in figure 1(a), with length $L = H$, width $W = H/4$ and resulting aspect ratios $\Gamma_x \equiv L/H = 1$ and $\Gamma_y \equiv W/H = 1/4$. The other two were 2-D rectangles with aspect ratios $\Gamma = L/H = 1$ and 10, respectively. Figure 1(b) shows the schematic diagram of the slip length *b* for the horizontal conducting plate. In all simulations, the horizontal plates were set to be slippery with $b \geqslant 0$, and the sidewalls were no-slip and adiabatic. All boundaries are rigid and impermeable. Thus, the dimensionless boundary conditions are given by

$$\hat{\boldsymbol{u}}\big|_{sidewalls} = 0, \tag{2.4}$$

$$\boldsymbol{n} \cdot \hat{\nabla} \hat{\theta}\big|_{sidewalls} = 0, \tag{2.5}$$

$$\hat{\boldsymbol{u}}\big|_{horizontal\,plates} = \hat{b} \partial_{\hat{z}} \hat{\boldsymbol{u}}, \tag{2.6}$$
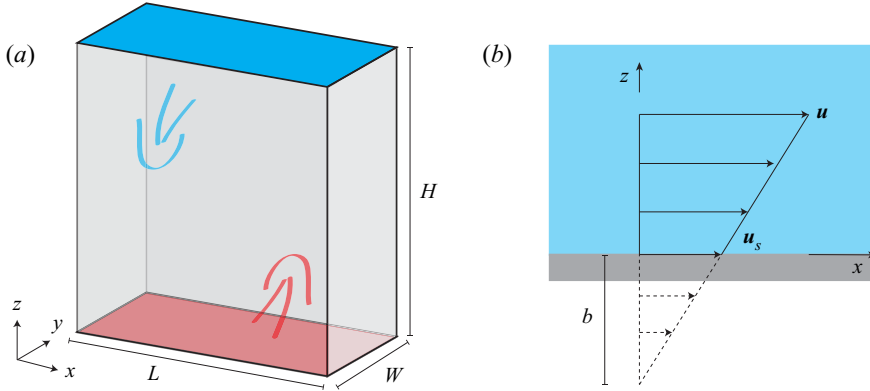
Figure 1. (*a*) Schematic diagram of the 3-D turbulent RBC sample used for numerical simulation. The dimensions of the sample are $L : H : W = 4 : 4 : 1$. (*b*) Schematic diagram of the slip length b and the velocity $u_s = b(\partial u/\partial n)_s$ on the surface.

$$\hat{v}\big|_{horizontal\,plates} = \hat{b}\partial_{\hat{z}}\hat{v}, \tag{2.7}$$

$$\hat{w}\big|_{horizontal\,plates} = 0, \tag{2.8}$$

$$\hat{\theta}\big|_{bottom} = 0.5, \quad \hat{\theta}\big|_{top} = -0.5, \tag{2.9a,b}$$

where $\hat{b} = b/H$ is the dimensionless slip length, and $\hat{u}$, $\hat{v}$ and $\hat{w}$ are, respectively, the velocity components along the x, y and z directions.

In the simulation, the governing equations were discretised by employing a conservative second-order central difference on a staggered grid in space. The time-derivative terms were discretised by the (implicit) backward Euler method. The diffusive terms were solved by an implicit scheme and the convective terms were solved by an explicit scheme. Inside the thermal BL, we used a small mesh size of $4 \times 10^{-4}\,H$ to ensure that there are at least 20 grid points to resolve the thermal BL. Outside the BL, we used a larger mesh size of $2 \times 10^{-3}\,H$ uniformly distributed along both the x and z directions. In all simulations, the initial conditions ($t = 0$) were set to $\hat{\boldsymbol{u}} = 0$ and $\hat{\theta} = 0$.

We calculated the dimensionless heat transport, the Nusselt number Nu, using $Nu \equiv \sqrt{Ra\,Pr}\,\langle\hat{w}\hat{\theta}\rangle_{V,t} + 1$. Here $\langle\cdot\rangle_{V,t}$ denotes volume and time averaging. In each simulation, we waited for a long enough time in the unit of T_f ($\gtrsim 100T_f$) so that the system reached a statistically steady state, and conducted time averaging after that (see table 2 in the Appendix). The overall running time ensured that all the averages are convergent. The minimum grid spacing was smaller than the dimensionless Kolmogorov length scale $\eta_K = \sqrt{Pr}/[Ra(Nu - 1)]^{1/4}$ and the Batchelor length scale $\eta_B = 1/[Ra(Nu - 1)]^{1/4}$ (Shishkina *et al.* 2010), which ensured adequate spatial resolution. Details of the DNS parameters can be found in table 2.

3. Global heat transport *Nu* for varying slip length *b*

Figure 2 shows typical snapshots of temperature fields (*a,c,e*) and velocity fields (*b,d,f*) for different values of b. The results are obtained from the 2-D sample with $\Gamma = 1$ and $Ra = 10^9$. For a plate of finite b, as shown in panels (*a–d*), the LSC of the fluid has a tilted single-roll mode with its axis along the sample diagonal. For free-slip plates, however, one
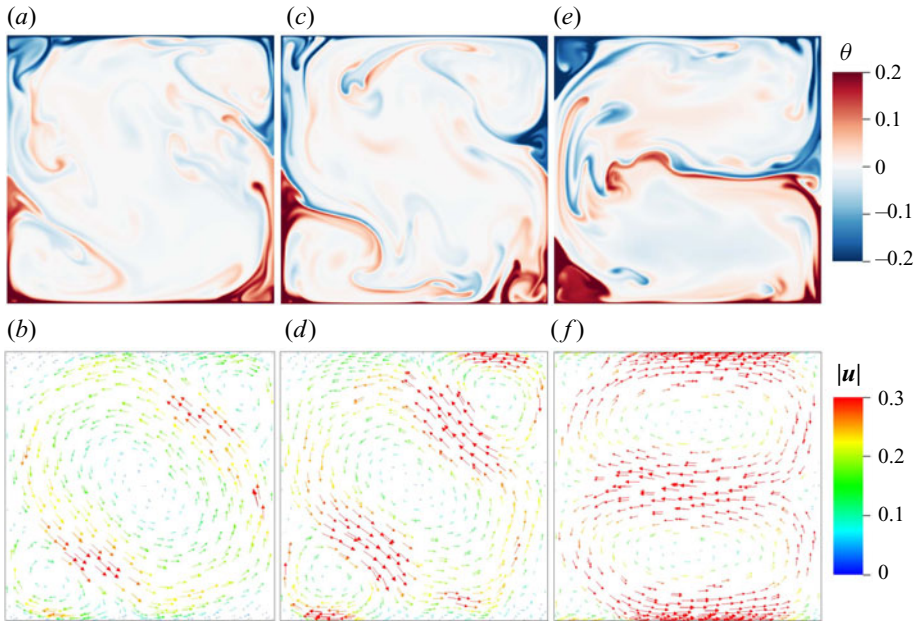
Figure 2. Snapshots of instantaneous (a,c,e) temperature and (b,d,f) velocity fields for no-slip plates (a,b), slippery plates with $b/\lambda_0 = 1.02$ (c,d) and free-slip plates (e,f). The DNS data are obtained for the 2-D RBC sample with $\Gamma = 1$ at $Ra = 10^9$.

can find a stable double-roll mode of the LSC – one roll on top of the other – in panels (e) and (f).

For comparison, as shown in figure 3, the LSC state for the 3-D sample remains the single-roll mode for both the no-slip and free-slip plates. Recent investigations for no-slip RBC revealed that the single-roll mode for water ($Pr \simeq 5$) can slightly enhance the heat transport compared to the double-roll mode (Xi & Xia 2008; Weiss & Ahlers 2011, 2013), and the enhancement becomes more prominent in low-Pr fluids and for multiple-roll LSC due to elliptical instability (Zwirner & Shishkina 2018; Zwirner, Tilgner & Shishkina 2020). With a similar mechanism, one would expect in free-slip RBC that the double-roll mode also transports less heat than the single-roll mode.

Figures 4(a) and 4(b) show, respectively, typical snapshots of the temperature and velocity fields from the 2-D sample with $\Gamma = 10$ and $Ra = 10^9$ for different b. For no-slip cases, as shown in figures 4(a1) and 4(b1), the number of LSC rolls R_n increases when Γ is stretched, and they form a stable multiple-roll mode – one roll next to the other – that filled up the closed sample. When R_n increases by 1, van der Poel *et al.* (2012) revealed that Nu increases by the amount of $\Delta Nu_{R_n}^{R_n+1}$, the value of which decreases as Γ increases until it saturates at a large Γ. For $Ra = 10^8$ and $\Gamma = 10$, our data show that $\Delta Nu_{R_n}^{R_n+1}$ is 2.5 % of Nu, which agrees well with the previous results by van der Poel *et al.* (2012). For $Ra = 10^9$, we find that $\Delta Nu_{R_n}^{R_n+1}$ is 1.4 % of Nu. Thus, the influence of the LSC roll number, if any, accounts for only a few per cent of Nu and decreases as Ra increases. With the fixed initial conditions of $\hat{\boldsymbol{u}} = 0$ and $\hat{\theta} = 0$, we found that the LSC roll number is rather stable and it rarely changes over the whole averaging time (see table 2).
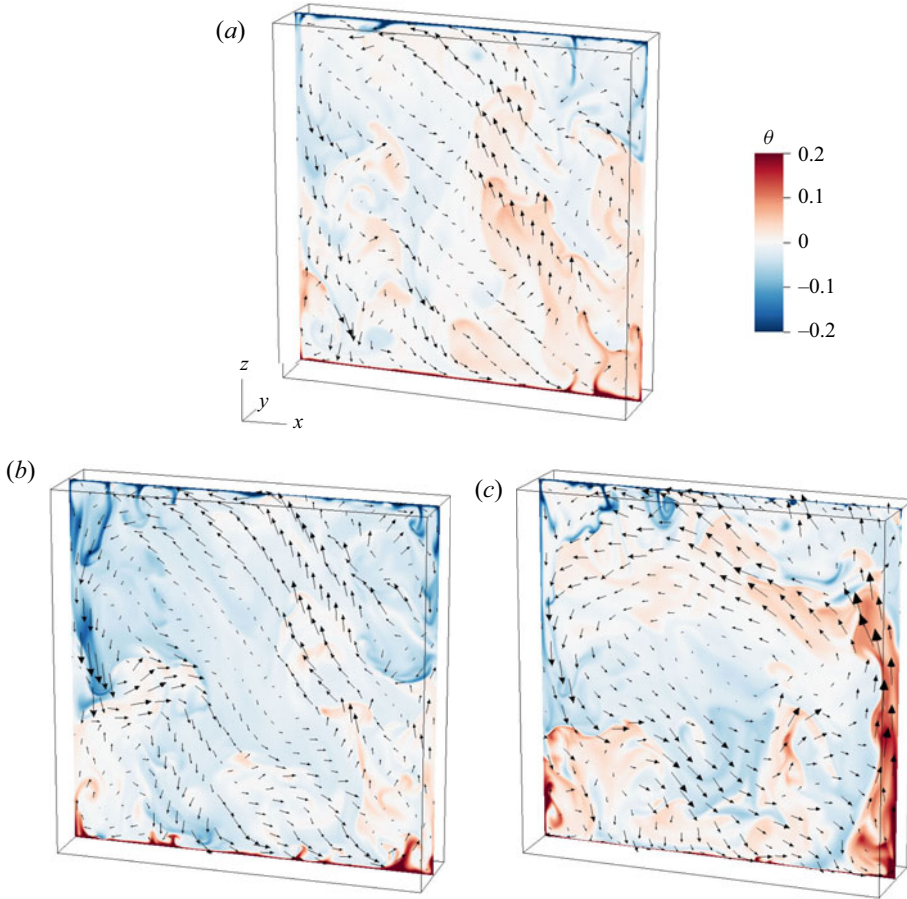
Figure 3. Snapshots of temperature and velocity fields in the 3-D sample with $\Gamma_y = 1/4$ and $Ra = 10^9$ for (*a*) no-slip plates, (*b*) slippery plates with $b/\lambda_0 = 1.02$ and (*c*) free-slip plates. The obtained fields are in the vertical plane of $y/W = 0.6$.

Figure 4(*a*2) and 4(*b*2) are the results for slippery plates with $b/\lambda_0 = 1.02$. It is found that R_n decrease as b increases. When the plates are free-slip, figures 4(*a*3) and 4(*b*3) show that the multiple-roll mode vanishes and the convection flow forms a single-roll circulation that spans the whole interior bulk region. Compared to the zonal flow that was observed in the DNS of free-slip RBC using a horizontally periodic boundary condition (Goluskin *et al.* 2014; Wang *et al.* 2020*a*), the single-roll LSC can move up and down along the vertical sidewalls. This flow motion helps enhance the vertical heat transport compared to the zonal flow, and thus yields higher efficiency of heat transport.

Now, we discuss the dependence of heat transport Nu on the slip length b. Figure 5(*a*) shows the reduced $Nu/Ra^{0.312}$ as a function of Ra obtained from the three closed samples for different values of the normalised b/H. We chose the scaling $Ra^{0.312}$ since it was well established in the classical RBC regime for $10^9 \lesssim Ra \lesssim 10^{12}$ (Ahlers *et al.* 2012*b*; He *et al.* 2012*b*). One can see in figure 5(*a*) that the classical scaling also roughly holds for different aspect ratios and for different values of b/H: only the prefactor increases as
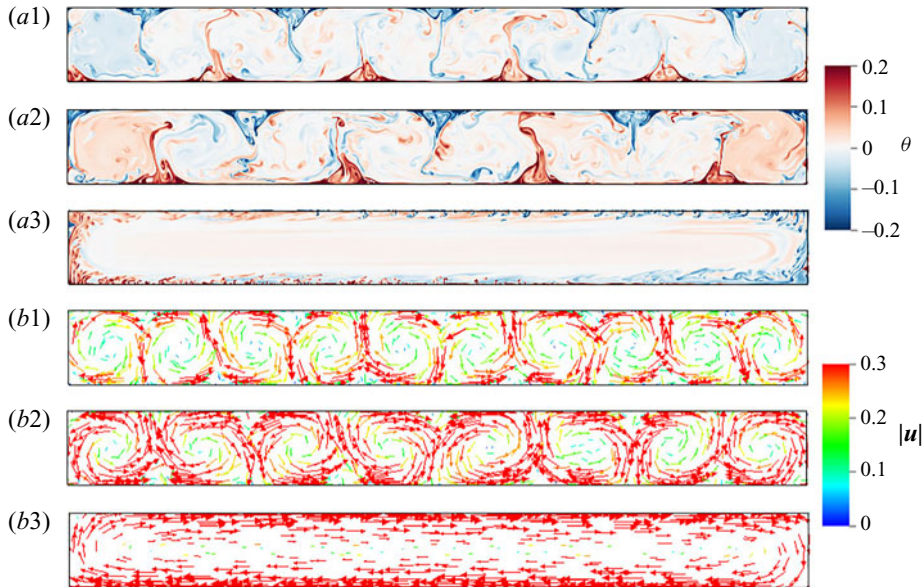
(*a*1)

(*a*2)

(*a*3)

θ

0.2
0.1
0
−0.1
−0.2

(*b*1)

(*b*2)

(*b*3)

$|\boldsymbol{u}|$

0.3
0.2
0.1
0

Figure 4. Snapshots of (*a*1–*a*3) temperature and (*b*1–*b*3) velocity fields obtained from the 2-D sample with $\Gamma = 10$ and $Ra = 10^9$. Results are for (*a*1,*b*1) no-slip plates, (*a*2,*b*2) slippery plates with $b/\lambda_0 = 1.02$ and (*a*3,*b*3) free-slip plates.

b/H increases, and reaches the maximal value when the plates are free-slip. The data (see table 2) show that the scalings of $Nu_F(Ra)$ for free-slip RBC in 2-D and 3-D are nearly the same, differing only by a constant factor. This is a consistent extension of previous results for no-slip RBC (van der Poel, Stevens & Lohse 2013).

We plot in figure 5(*b*) the ratio Nu_F/Nu_0 as a function of Ra for different Γ. Here Nu_0 and Nu_F represent the normalised heat flux for no-slip and free-slip plates, respectively. In the 2-D sample with $\Gamma = 1$, we find $Nu_F/Nu_0 \simeq 1.8$ nearly independent of Ra, and the ratio is $\sim 6\%$ lower than those in the other two samples, where the LSC for free-slip plates remains the single-roll mode. As discussed above, such small deviations are largely attributed to different roll modes of the LSC, while the effects of the slippery plates on Nu are essentially the same in both 2-D and 3-D closed RBC.

Figure 5(*c*) shows the results for Nu/Nu_0 with $\Gamma = 1$. It is found that the Nu data for different Ra and b collapse onto a single master curve once b is rescaled by λ_0. Here $\lambda_0 \equiv H/(2Nu_0)$ is the thermal BL thickness for no-slip plates. Over the studied parameter range, all the Nu/Nu_0 data closely follow the function $Nu/Nu_0 = N_0 \tanh(b/\lambda_0) + 1$, with $N_0 = 0.8 \pm 0.03$.

4. Temperature boundary-layer profiles in slippery RBC

4.1. *Equations of the mean temperature and temperature variance profiles*

In this section, we derive equations for the dimensionless profiles of the mean temperature Θ and temperature variance Ω near the BL in slippery RBC. The method is based on the ideas in previous studies for no-slip RBC (Shishkina *et al.* 2015; Wang *et al.* 2018).

We consider a quasi-2-D convective flow over an infinite horizontal plate. With the Reynolds decomposition and the BL approximation, one obtains the mean temperature
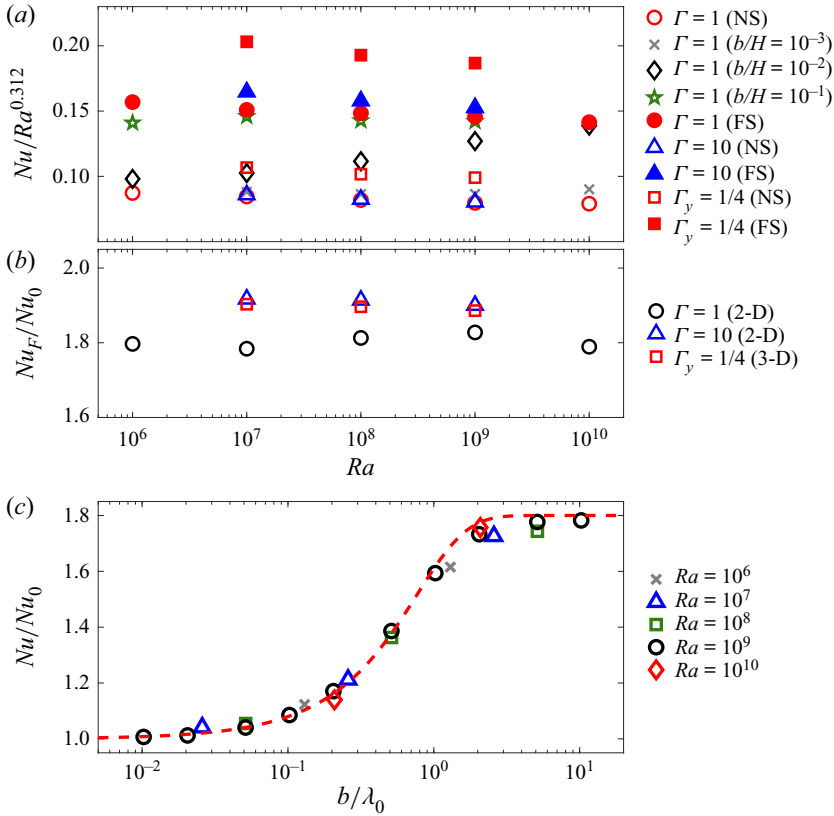
Figure 5. (*a*) Plot of $Nu/Ra^{0.312}$ as a function of Ra from 2-D and 3-D DNS for different Γ and b/H. Symbols correspond to $\Gamma = 1$ with no-slip plates (red open circles), $b/H = 10^{-3}$ (grey crosses), $b/H = 10^{-2}$ (black open diamonds), $b/H = 10^{-1}$ (green stars) and free-slip plates (red solid circles). Blue open (solid) triangles are for $\Gamma = 10$ with no-slip (free-slip) plates. Red open (solid) squares are for $\Gamma_y = 1/4$ with no-slip (free-slip) plates. (*b*) Plot of Nu_F/Nu_0 as a function of Ra in 2-D and 3-Dsamples for $\Gamma = 1$ (black circles), $\Gamma = 10$ (blue triangles) and $\Gamma_y = 1/4$ (red squares). (*c*) Plot of Nu/Nu_0 as a function of b/λ_0 on a logarithmic scale. The DNS data are obtained in the 2-D sample with $\Gamma = 1$ for varying $Ra = 10^6$ (grey crosses), 10^7 (blue triangles), 10^8 (green squares), 10^9 (black circles) and 10^{10} (red diamonds). The red dashed line represents the function $Nu/Nu_0 = N_0 \tanh(b/\lambda_0) + 1$, with $N_0 = 0.8$. Here Nu_0 and Nu_F represent the normalised heat flux for no-slip and free-slip plates, respectively; and $\lambda_0 \equiv H/(2Nu_0)$ is the thermal BL thickness accordingly.

BL equation,

$$\langle u\rangle\partial_x\langle\theta\rangle + (\langle w\rangle - \partial_z\kappa_t)\partial_z\langle\theta\rangle = (\kappa + \kappa_t)\partial_z^2\langle\theta\rangle, \tag{4.1}$$

with the eddy thermal diffusivity

$$\kappa_t = -\langle w'\theta'\rangle/\partial_z\langle\theta\rangle. \tag{4.2}$$

Here and below, $\langle\cdot\rangle$ denotes average over time; $\langle\theta\rangle$, $\langle u\rangle$ and $\langle w\rangle$ are long-time averages of temperature, horizontal velocity and vertical velocity, respectively; and $\theta'(x, z, t)$, $u'(x, z, t)$ and $w'(x, z, t)$ are their fluctuations. For an incompressible fluid, the continuity equation is

$$\partial_x u' + \partial_z w' = 0. \tag{4.3}$$

943 A2-9

On the slippery plate with $z = 0$ and $b > 0$, both θ' and v' vanish, while u' and $\partial_x u'$ exist, leading to $\partial_z w' \neq 0$. Thus, one has

$$\langle w'\theta' \rangle = \partial_z \langle w'\theta' \rangle = 0 \tag{4.4}$$

and

$$\partial_z^2 \langle w'\theta' \rangle \neq 0. \tag{4.5}$$

Using the dimensionless length $\xi = z/\lambda$, with $\lambda \equiv H/(2Nu)$ being the thermal BL thickness near the slippery plate, one finds that κ_t and its derivatives with respect to ξ vanish at the plate, i.e.

$$\kappa_t \big|_{\xi=0} = (\kappa_t)_\xi \big|_{\xi=0} = 0, \quad (\kappa_t)_{\xi\xi} \big|_{\xi=0} \neq 0. \tag{4.6a,b}$$

For small ξ, κ_t can be approximated by

$$\kappa_t/\kappa \approx m\xi^p, \tag{4.7}$$

with a dimensionless constant $m > 0$ and an effective exponent $p \geqslant 2$ varying with the degree of slippage. For $Pr > 1$, the solution of (4.1) is given by (Shishkina *et al.* 2015)

$$\Theta(\xi) \equiv \frac{\theta_{bottom} - \langle \theta(\xi) \rangle}{\Delta/2} = \int_0^\xi (1 + m\eta^p)^{-c} \, \mathrm{d}\eta, \tag{4.8}$$

where $c \geqslant 1$ is a parameter satisfying $\Theta(\infty) = 1$, and thus

$$m = [\Gamma(1/p)\Gamma(c - 1/p)/(p\Gamma(c))]^p, \tag{4.9}$$

where $\Gamma(\cdot)$ denotes the gamma function. It is noteworthy that (4.7) to (4.9) determine a general form of the mean temperature profiles $\Theta(\xi)$ in slippery RBC with different b. When $b \to \infty$ for free-slip plates, the leading term in (4.7) yields $p = 2$. When $b = 0$, all terms in (4.6a,b) vanish on the no-slip plates at $\xi = 0$. It leads to $p = 3$ and the corresponding $\Theta(\xi)$ profiles that are the same as the previous results found by Shishkina *et al.* (2015). In a more general case, the value of p is expected to be between 2 and 3.

The dimensionless form of temperature variance $\eta = \langle \theta'^2 \rangle$ is defined by

$$\Omega \equiv \eta/\eta_0. \tag{4.10}$$

Here η_0 is the maximal value of η. In the BL, the equation of Ω is given by (Wang *et al.* 2016)

$$\eta_0(\langle u \rangle \partial_x \Omega + \langle w \rangle \partial_z \Omega) - 2\kappa_t(\partial_z \langle \theta \rangle)^2 - \partial_z(\kappa_f \partial_z \eta) = \kappa \eta_0 \partial_z^2 \Omega - 2\epsilon_\theta, \tag{4.11}$$

with the thermal dissipation rate

$$\epsilon_\theta = \kappa[\langle (\partial_x \theta')^2 \rangle + \langle (\partial_z \theta')^2 \rangle] \tag{4.12}$$

and the turbulent diffusivity for temperature variance,

$$\kappa_f = -\langle w'\theta'^2 \rangle / \partial_z \eta. \tag{4.13}$$

Since both θ' and θ'^2 are advected by the same local velocity u', one would expect that the effects of the BL fluctuations on them are similar. Thus on the slippery plates at $\xi = 0$, κ_f can be approximated by

$$\kappa_f/\kappa \approx n\xi^p, \tag{4.14}$$

with the prefactor $n > 0$.

943 A2-10

Using (4.14) and the mean temperature equation (4.8) above, one can write the three terms on the left-hand side of (4.11) as follows:

$$\eta_0(\langle u \rangle \partial_x \Omega + \langle w \rangle \partial_z \Omega) = -\frac{\eta_0 \kappa}{\lambda^2} \beta \xi^{p-1} \frac{\mathrm{d}\Omega(\xi)}{\mathrm{d}\xi}, \tag{4.15}$$

$$-2\kappa_t (\partial_z \langle \theta \rangle)^2 = -\kappa \frac{\Delta^2}{2\lambda^2} \frac{m\xi^p}{(1 + m\xi^p)^{2c}} \tag{4.16}$$

and

$$-\partial_z(\kappa_f \partial_z \eta) = -np\xi^{p-1}\kappa\eta_0 \frac{\partial \Omega(\xi)}{\partial \xi} \frac{1}{\lambda^2} - n\xi^p \kappa \eta_0 \frac{\partial^2 \Omega(\xi)}{\partial \xi^2} \frac{1}{\lambda^2}, \tag{4.17}$$

where $\beta = pm(c - 1)$.

The right-hand side of (4.11) can be written as

$$\kappa \eta_0 \partial_z^2 \Omega = \kappa \eta_0 \frac{\partial^2 \Omega(\xi)}{\partial \xi^2} \frac{1}{\lambda^2} \tag{4.18}$$

and

$$-2\epsilon_\theta = -2\kappa \frac{\eta_0}{\lambda^2} \left[\frac{1}{4} \frac{[\mathrm{d}\Omega(\xi)/\mathrm{d}\xi]^2}{\Omega(\xi)} + \gamma \Omega(\xi) \right]. \tag{4.19}$$

Here $\gamma = 2\lambda^2(1/l_x^2 + 1/l_z^2)$, with l_x and l_z being the Taylor microscales of temperature fluctuations in the x and z directions, respectively.

Taking (4.15) to (4.19) into (4.11), one obtains a general ordinary differential equation of Ω for slippery RBC:

$$(1 + n\xi^p) \frac{\mathrm{d}^2 \Omega(\xi)}{\mathrm{d}\xi^2} + (\beta + np)\xi^{p-1} \frac{\mathrm{d}\Omega(\xi)}{\mathrm{d}\xi} - \frac{[\mathrm{d}\Omega(\xi)/\mathrm{d}\xi]^2}{2\Omega(\xi)}$$

$$+ \frac{\Delta^2}{2\eta_0} \frac{m\xi^p}{(1 + m\xi^p)^{2c}} - 2\gamma \Omega(\xi) = 0. \tag{4.20}$$

Note that for $p = 3$, (4.20) is equivalent to equation (20) in Wang *et al.* (2016) for no-slip plates.

With the initial conditions $\Omega(\xi_0) = 1$ and $\mathrm{d}\Omega(\xi_0)/\mathrm{d}\xi = 0$ at the peak position ξ_0 of $\Omega(\xi)$, (4.20) yields the solution $\Omega(\xi; p, c, \Delta^2/\eta_0, n, \gamma)$ for the general form of temperature variance profiles $\Omega(\xi)$ near the plate. The values of the maximal normalised temperature variance Δ^2/η_0 and the peak position ξ_0 can be obtained directly from the temperature data. The values of $\gamma \simeq 1$ and $\xi_0 \simeq 0.85$ were found for $Pr = 4.4$ and 7.6 in 3-D experiments and DNS (Wang *et al.* 2016, 2018), and they depend weakly on Pr and the sample geometry. The parameters p, c and n are determined by the fits of (4.7), (4.8) and (4.14) to the temperature data.

4.2. *DNS data for the mean temperature and temperature variance*

Figure 6(*a*) shows the normalised turbulent diffusivities κ_t/κ for the temperature fluctuation θ' as a function of ξ. The DNS data were obtained from the 2-D sample with $\Gamma = 1$ and the 3-D sample with $\Gamma_y = 1/4$. Over the studied Ra range $10^6 \leqslant Ra \leqslant 10^{10}$, the κ_t/κ data from different samples fall into two distinct groups: one for no-slip plates and the other for free-slip plates. For $\xi \lesssim 1$, we find the two groups of data closely follow the
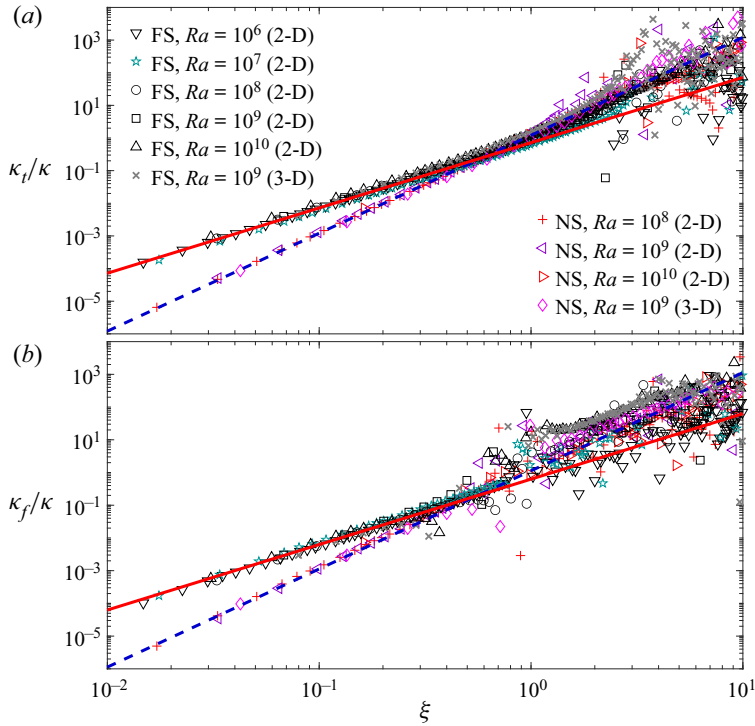
Figure 6. Normalised turbulent diffusivities (*a*) κ_t/κ and (*b*) κ_f/κ as a function of ξ in logarithmic scales for no-slip (NS) and free-slip (FS) horizontal plates. The DNS data are obtained from the 2-D sample with $\Gamma = 1$ and the 3-D sample with $\Gamma_y = 1/4$ for different *Ra*. The two lines in panel (*a*) represent the power function $\kappa_t/\kappa = m\xi^p$ with the parameters $m = 0.73$, $p = 2$ (red solid line) and $m = 0.85$, $p = 3$ (blue dashed line). In panel (*b*) they represent the power function $\kappa_f/\kappa = n\xi^p$ with $n = 0.85$, $p = 2$ (red solid line) and $n = 1.13$, $p = 3$ (blue dashed line).

power function $\kappa_t/\kappa = m\xi^p$ from (4.7) with different values of *m* and *p*. For no-slip plates, the value $p = 3$ is consistent with previous DNS results obtained in a 3-D cylindrical sample (Shishkina *et al.* 2015) and a thin disk (Wang *et al.* 2018). The value $m = 0.85$ is close to the thin disk ($m = 0.8$), but about 1.5 times lower than the cylindrical sample, indicating relatively less BL fluctuations in the 2-D or quasi-2-D convection flows. For free-slip plate, our result shows $p = 2$, which agrees with the predicted value in § 4.1.

Figure 6(*b*) shows the results of normalised turbulent diffusivity κ_f/κ for the temperature variance $\overline{\theta'^2}$ obtained from the same simulations as those for κ_t/κ. It is found that the κ_f/κ data in the two RBC samples for different *Ra* also fall into two groups. Over the range $\xi \lesssim 1$, the no-slip data closely follow the power function $\kappa_f/\kappa = 1.13\xi^3$, which is consistent with the previous results in the thin disk (Wang *et al.* 2018). For free-slip plates, the κ_f/κ data are found to be well described by the power function $\kappa_f/\kappa = 0.85\xi^2$.

Figures 7(*a*) and (*b*) show similar results of κ_t/κ and κ_f/κ, respectively, for different values of *b*. All the data were obtained from the 2-D sample with $\Gamma = 1$ and $Ra = 10^9$. In both panels, the diffusivities are compensated by ξ^2 in order to present an enlarged view of their evolution as the dimensionless slip length b/H. In the BL for $\xi \lesssim 0.6$, both κ_t/κ and κ_f/κ follow a power-law scaling of ξ^p, with the exponent *p* varying monotonically from 3 to 2 as b/H increases from 0 to ∞. For a given *b*, one sees that the scaling exponents
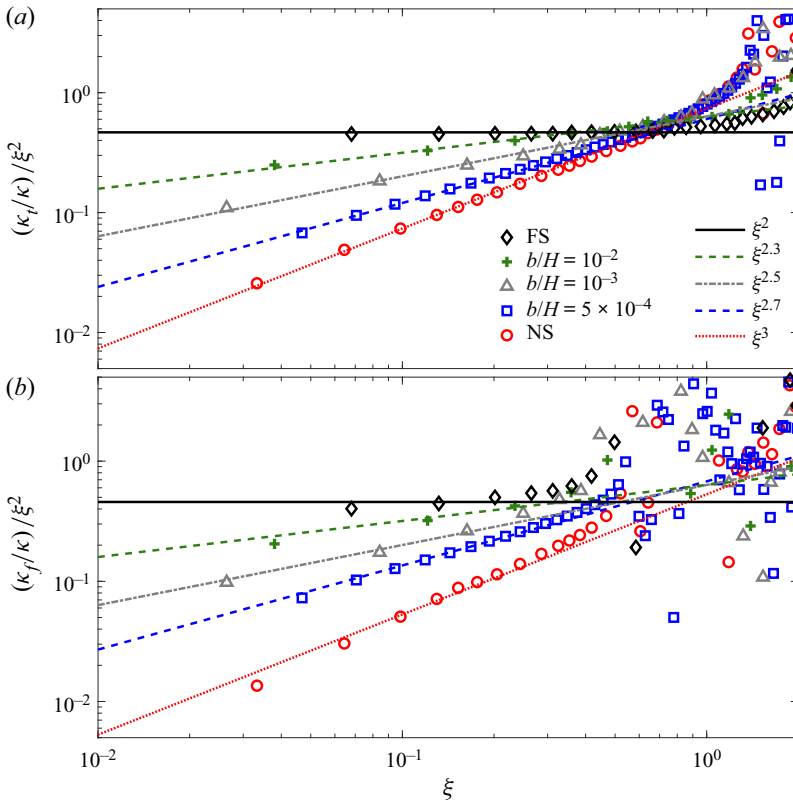
Figure 7. Normalised turbulent diffusivities (a) κ_t/κ and (b) κ_f/κ as a function of ξ for slippery horizontal plates with varying b/H. The DNS data are obtained from the 2-D sample with $\Gamma = 1$ and $Ra = 10^9$. The symbols in the two panels indicate data for different values of $b/H = 0$ (red circles), 5×10^4 (blue squares), 10^{-3} (grey triangles), 10^{-2} (green pluses) and for free-slip plates (black diamonds). The lines in the two panels represent the power functions $\kappa_t/\kappa = m\xi^p$ and $\kappa_f/\kappa = n\xi^p$, respectively, with the effective exponent (from top to bottom near the left edge) $p = 2.0, 2.3, 2.5, 2.7$ and 3.0.

for both diffusivities are the same. This is consistent with the assumption made above, in which the BL fluctuations have similar effects on both θ' and θ'^2.

Thus, both figures 6 and 7 show that the turbulent diffusivities κ_t/κ and κ_f/κ in the BL can be approximated by the power-law scaling in (4.7) and (4.14), respectively. For different values of b, we obtain the exponent p from the fits of (4.7) and (4.14) to the $\Gamma = 1$ data in the range $10^7 \leqslant Ra \leqslant 10^{10}$, and show p as a function of b/λ_0 in figure 8. The result shows that for $b/\lambda_0 \lesssim 0.03$ the obtained exponent $p = 3$, which indicates that the temperature BL profiles remain roughly the same as those for no-slip plates. In the range $0.03 \lesssim b/\lambda_0 \lesssim 10$, the exponent decreases monotonically from $p = 3$ to $p = 2$ as b/λ_0 increases. This demonstrates a gradual change of the BL fluctuation intensity from no-slip to free-slip boundaries. The accompanying Nu increment, as shown in figure 5(c), accounts for $\sim 97\%$ of the total heat flux increment due to the boundary condition change. When b/λ_0 is beyond 10, we have $p = 2$, and in this case the temperature BL profiles, as well as the heat flux, are nearly the same as those for free-slip plates.
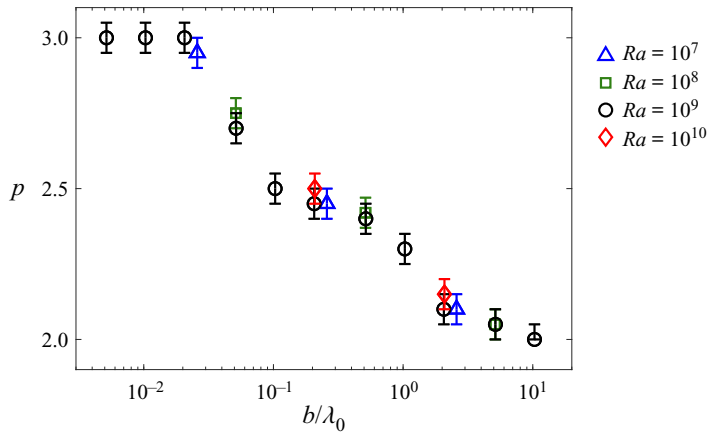
Figure 8. Dependence of the exponent p on the normalised slip length b/λ_0 in semi-log scales. The DNS data are obtained in the $\Gamma = 1$ sample with different $Ra = 10^7$ (blue triangles), 10^8 (green squares), 10^9 (black circles) and 10^{10} (red diamonds).

b/λ_0	p	c	m	Δ^2/η_0	n	γ	ξ_0
0	3.00 ± 0.05	1.20 ± 0.02	1.21 ± 0.02	89.2 ± 0.4	1.13 ± 0.02	0.91 ± 0.01	0.85 ± 0.05
0.10	2.50 ± 0.05	1.40 ± 0.02	1.00 ± 0.02	96.0 ± 0.4	0.96 ± 0.02	1.00 ± 0.01	0.85 ± 0.05
1.02	2.30 ± 0.05	1.47 ± 0.02	0.96 ± 0.02	104.0 ± 0.4	0.90 ± 0.02	1.40 ± 0.01	0.85 ± 0.05
∞	2.00 ± 0.05	1.80 ± 0.02	0.73 ± 0.02	124.4 ± 0.4	0.85 ± 0.02	1.46 ± 0.01	0.85 ± 0.05

Table 1. Values of the parameters used to calculate $\Theta(\xi)$ and $\Omega(\xi)$ that are shown in figures 9 and 10.

Table 1 lists the exponent p and other equation parameters for different b/λ_0. With these values, one can calculate the general equations for the mean temperature profiles $\Theta(\xi)$ and the temperature variance profiles $\Omega(\xi)$ using (4.8) and (4.20), respectively.

Finally, we turn to the DNS results for the mean temperature Θ and temperature variance Ω, and examine the predicted equations for their BL profiles. Figure 9(a) shows $\Theta(\xi)$ as a function of ξ obtained from the 2-D sample with $\Gamma = 1$ and the 3-D sample with $\Gamma_y = 1/4$ at different Ra. It is found that the $\Theta(\xi)$ data fall into two groups – one for no-slip plates and the other for free-slip plates – both independent of Ra and the sample geometry. With the values of m and p obtained from figure 6(a), we calculated the $\Theta(\xi)$ curves using the predicted equations (4.8) and (4.9), and plot them in figure 9(a). It is clearly seen that, for either no-slip or free-slip plates, the calculated $\Theta(\xi)$ curve can well describe the DNS data for ξ up to 3.

Figure 9(b) shows the corresponding $\Omega(\xi)$ as a function of ξ from the same DNS as in figure 9(a). Similar to the results of $\Theta(\xi)$, the $\Omega(\xi)$ profiles for no-slip and free-slip plates are overlapped respectively onto two separate groups, which are independent of Ra and the sample shape. The two groups of datasets have nearly the same peak position $\xi_0 = 0.85$. In figure 9(b), we also plot the numerical solutions $\Omega(\xi; p, c, \Delta^2/\eta_0, n, \gamma)$ of (4.20) with $\xi_0 = 0.85$ and the other parameters listed in table 1. It is seen that the predicted $\Omega(\xi)$ curves for no-slip and free-slip plates can well fit the corresponding DNS data for $\xi \lesssim 1.5$. Beyond $\xi \simeq 2$, the predicted curves start to deviate from the data because the power-law scaling of κ_f/κ no longer holds.
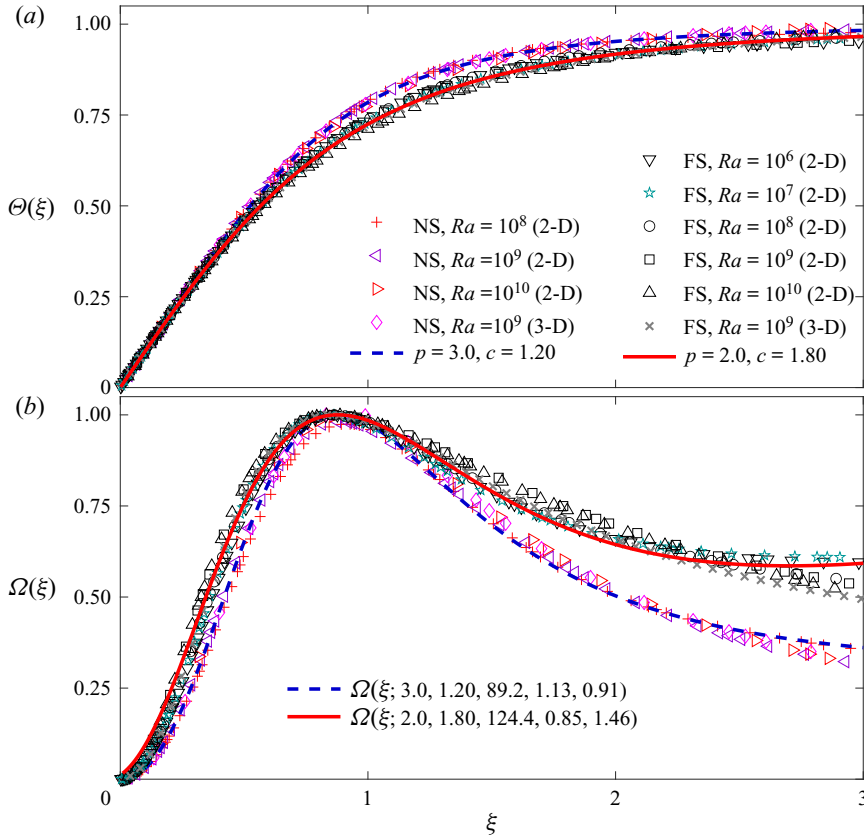
943 A2-14

Figure 9. Plots of (*a*) Θ and (*b*) Ω as functions of ξ obtained in the DNS for different Ra from the 2-D sample with $\Gamma = 1$ and the 3-D sample with $\Gamma_y = 1/4$. The red solid and blue dashed lines in panel (*a*) represent the calculated $\Theta(\xi)$ using (4.8). In panel (*b*), they are the numerical solutions $\Omega(\xi; p, c, \Delta^2/\eta_0, n, \gamma)$ of (4.20) with $\xi_0 = 0.85$. The values of the parameters used to calculate $\Theta(\xi)$ and $\Omega(\xi)$ are listed in table 1.

To further examine the predicted general temperature equations (4.8) and (4.20) for slippery plates, we show in figures 10(*a*) and 10(*b*), respectively, the $\Theta(\xi)$ and $\Omega(\xi)$ BL profiles for varying slip lengths b/λ_0. All the DNS temperature data were obtained from the 2-D samples with $\Gamma = 1$ and 10 at $Ra = 10^9$. We also calculated the $\Theta(\xi)$ and $\Omega(\xi)$ data from (4.8) and (4.20) with the parameters listed in table 1, and plot them in figures 10(*a*) and 10(*b*), respectively. Excellent agreements are found between the predicted temperature BL profiles and the temperature data for varying Γ and b/λ_0. It is noted that all the parameters used in the temperature equations depend only on the slip length b, and there are no additional adjustable parameters in the calculations of $\Theta(\xi)$ and $\Omega(\xi)$. As summarised in table 1, the peak position ξ_0 for $\Omega(\xi)$ remains the same, while all other parameters in the predicted temperature forms change monotonically with b/λ_0.

In figure 10(*a*), one sees that the $\Theta(\xi)$ BL profiles obtained from the $\Gamma = 10$ sample for both no-slip and free-slip plates agree well with the corresponding $\Theta(\xi)$ curves calculated using (4.8). The calculated $\Theta(\xi)$ curves are the same as those in figure 9(*a*) for the other two samples. Similar agreements are also found in figure 10(*b*) for the $\Omega(\xi)$ data. The results indicate that the influences of the slippery plates on both mean temperature and temperature variance profiles remain the same in the three samples over the studied
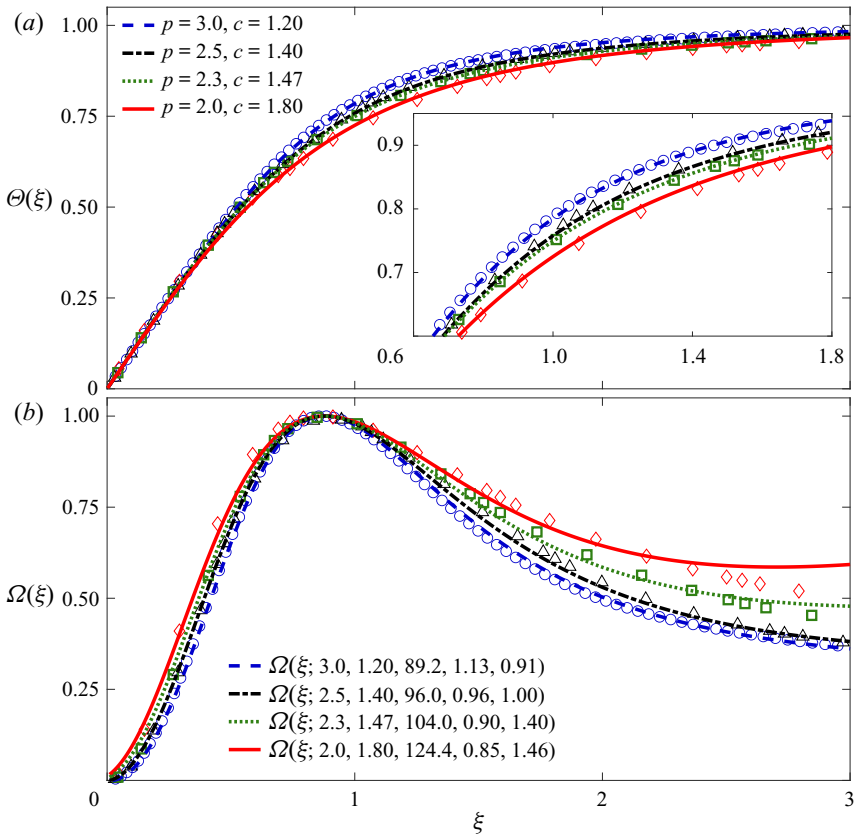
Figure 10. Similar results as in figure 9 for (*a*) Θ and (*b*) Ω, obtained from the 2-D samples with $\Gamma = 1$ and 10. The various symbols in the two panels correspond to different Γ and b/λ_0: red diamonds, $\Gamma = 10$, free-slip plates; green squares, $\Gamma = 1$, $b/\lambda_0 = 1.02$; black triangles, $\Gamma = 1$, $b/\lambda_0 = 0.10$; and blue circles, $\Gamma = 10$, no-slip plates. The lines in panel (*a*) represent (4.8), and those in panel (*b*) are the solutions $\Omega(\xi; p, c, \Delta^2/\eta_0, n, \gamma)$ of (4.20) with $\xi_0 = 0.85$. The inset in panel (*a*) shows an enlarged view. The values of the parameters used to calculate $\Theta(\xi)$ and $\Omega(\xi)$ are listed in table 1. All the data are obtained at $Ra = 10^9$ and $Pr = 4.3$.

Ra range. One would expect that such influences have a weak dependence on the sample geometry and *Ra*, but rather would be dominated by the slip length of the plates. Thus the predicted equations (4.8) and (4.20) for the temperature BL profiles are expected to be valid in a class of thermal convection flows with slippery conducting plates.

5. Summary

We have carried out a systematic DNS study of the Nusselt number and the temperature BL profiles in turbulent Rayleigh–Bénard convection with slippery horizontal conducting plates. The slip length *b* of the plates varied from 0 for no-slip to ∞ for free-slip plates. The DNS were conducted in the *Ra* range $10^6 \leqslant Ra \leqslant 10^{10}$ and for a fixed $Pr = 4.3$. Three closed samples were used in the DNS. One is a 3-D cuboid sample with the dimension of $L : H : W = 4 : 4 : 1$ and the other two are 2-D rectangular samples with $\Gamma = 1$ and 10, respectively.

For a given $b > 0$, the obtained *Nu* data for slippery RBC approximately follow the classical *Nu* scaling that is observed in no-slip RBC, differing only by an increasing

prefactor as b increases. The reduced heat transport Nu/Nu_0 from the three samples for different Ra and b can be overlapped onto a single master curve, once the slip length b is normalised by the thermal BL thickness $\lambda_0 \equiv H/(2Nu_0)$. Our DNS results show that the overlapped Nu/Nu_0 data follow the scaling $Nu/Nu_0 = N_0 \tanh(b/\lambda_0) + 1$, with $N_0 = 0.8 \pm 0.03$. This indicates that the slip length can be used as an appropriate characteristic length scale to calculate the heat transport enhancement in slippery RBC.

Near the BL, we calculated the turbulent diffusivities κ_t for the temperature fluctuations θ' and κ_f for the temperature variance θ'^2. The data were obtained from the three closed samples for different Ra and b. It is found that both κ_t and κ_f can be approximated by a power-law scaling $\sim \xi^p$, with an effective scaling exponent p varying from 3 for no-slip to 2 for free-slip plates. These results suggest that the influences of BL fluctuations on both θ' and θ'^2 are similar, and show the evolution of such influences as a varying slip length. For $b/\lambda_0 \lesssim 0.03$, we find $p = 3$ and the corresponding temperature profiles $\Theta(\xi)$ and $\Omega(\xi)$ remain roughly the same as those for no-slip plates. In the range $0.03 \lesssim b/\lambda_0 \lesssim 10$, our results indicate that the BL fluctuation intensity gradually increases from no-slip to free-slip cases, which accounts for $\sim 97\%$ of the total Nu enhancement as b/λ_0 increases. When $b/\lambda_0 \gtrsim 10$, the obtained $\Theta(\xi)$, $\Omega(\xi)$ and Nu are nearly the same as those for free-slip plates. The analytical relationship between the exponent p and the slip length b is worthy of further investigations in the future.

From these findings, we derived general equations (4.8) and (4.20) for the temperature BL profiles of Θ and Ω, respectively, in slippery RBC with $b \geqslant 0$. When $b = 0$, the predicted temperature BL profiles are consistent with previous results for no-slip RBC (Shishkina *et al.* 2015; Wang *et al.* 2016). When $b > 0$, they are in excellent agreement with our DNS data obtained from different samples with varying Ra and b. Our work thus provides general functional forms of Nu/Nu_0, Θ and Ω across the BL in slippery RBC. The predicted forms represent the essential effects from the slippery plates on the heat transport and temperature BL profiles, which have weak dependence on the sample geometry and Ra in the studied range. We expect that these scaling forms can be applied to a class of thermal convection flows with slippery conducting plates, ranging from industrial applications to geophysical turbulence.

Author ORCIDs.
 Yin Wang https://orcid.org/0000-0002-6572-4902;
 Xiaozhou He https://orcid.org/0000-0001-8116-889X.

Appendix

Details of the DNS parameters and datasets calculated in the numerical studies are given in table 2.

Γ	Ra	b/H	b/λ	τ_f	$N_x \times N_z$	$N_x \times N_y \times N_z$	Nu
1 (2-D)	10^6	0	0	1000	512×576	—	6.50
1 (2-D)	10^6	10^{-2}	0.13	1000	512×576	—	7.30
1 (2-D)	10^6	10^{-1}	1.30	1000	512×576	—	10.50
1 (2-D)	10^6	∞	∞	1000	512×576	—	11.68
1 (2-D)	10^7	0	0	1000	512×576	—	12.92
1 (2-D)	10^7	10^{-3}	0.03	1000	512×576	—	13.45
1 (2-D)	10^7	10^{-2}	0.26	1000	512×576	—	15.66
1 (2-D)	10^7	10^{-1}	2.58	1000	512×576	—	22.30
1 (2-D)	10^7	∞	∞	1000	512×576	—	23.05
1 (2-D)	10^8	0	0	1000	512×576	—	25.65
1 (2-D)	10^8	10^{-3}	0.05	1000	512×576	—	27.06
1 (2-D)	10^8	10^{-2}	0.51	1000	512×576	—	34.96
1 (2-D)	10^8	10^{-1}	5.13	1000	512×576	—	44.72
1 (2-D)	10^8	∞	∞	1000	512×576	—	46.50
1 (2-D)	10^9	0	0	500	1024×1152	—	51.22
1 (2-D)	10^9	10^{-4}	0.01	500	1024×1152	—	51.57
1 (2-D)	10^9	2×10^{-4}	0.02	500	1024×1152	—	51.85
1 (2-D)	10^9	5×10^{-4}	0.05	500	1024×1152	—	53.29
1 (2-D)	10^9	10^{-3}	0.10	500	1024×1152	—	55.59
1 (2-D)	10^9	2×10^{-3}	0.20	500	1024×1152	—	59.97
1 (2-D)	10^9	5×10^{-3}	0.51	500	1024×1152	—	71.00
1 (2-D)	10^9	10^{-2}	1.02	500	1024×1152	—	81.62
1 (2-D)	10^9	2×10^{-2}	2.05	500	1024×1152	—	88.75
1 (2-D)	10^9	5×10^{-2}	5.12	500	1024×1152	—	91.00
1 (2-D)	10^9	10^{-1}	10.24	500	1024×1152	—	91.29
1 (2-D)	10^9	∞	∞	500	1024×1152	—	93.61
1 (2-D)	10^{10}	0	0	500	1024×1152	—	104.02
1 (2-D)	10^{10}	10^{-3}	0.21	500	1024×1152	—	118.76
1 (2-D)	10^{10}	10^{-2}	2.08	500	2048×2304	—	183.09
1 (2-D)	10^{10}	∞	∞	500	2048×2304	—	186.45
10 (2-D)	10^7	0	0	500	5120×576	—	13.12
10 (2-D)	10^7	∞	∞	500	5120×576	—	25.15
10 (2-D)	10^8	0	0	500	5120×576	—	25.83
10 (2-D)	10^8	∞	∞	500	5120×576	—	49.44
10 (2-D)	10^9	0	0	500	5120×576	—	51.62
10 (2-D)	10^9	∞	∞	500	$10\,240 \times 1152$	—	98.08
1/4 (3-D)	10^7	0	0	250	—	$512 \times 64 \times 576$	16.30
1/4 (3-D)	10^7	∞	∞	250	—	$512 \times 64 \times 576$	31.02
1/4 (3-D)	10^8	0	0	250	—	$512 \times 64 \times 576$	31.86
1/4 (3-D)	10^8	∞	∞	250	—	$512 \times 64 \times 576$	60.42
1/4 (3-D)	10^9	0	0	250	—	$512 \times 64 \times 576$	63.64
1/4 (3-D)	10^9	∞	∞	250	—	$1024 \times 128 \times 1152$	120.02

Table 2. The DNS parameters and calculated datasets in the numerical studies. The columns from left to right indicate parameters in the conducted DNS of three RBC samples: Γ, Ra, the dimensionless slip length b/H and b/λ (with λ being the thermal BL thickness), the averaging time τ_f in free-fall time units, the number of nodes in each direction of the computational mesh in 2-D ($N_x \times N_z$) and 3-D ($N_x \times N_y \times N_z$) cases, together with the obtained Nu.

<div align="center">REFERENCES</div>

AHLERS, G. 2009 Turbulent convection. *Physics* **2**, 74.

AHLERS, G., BODENSCHATZ, E., FUNFSCHILLING, D., GROSSMANN, S., HE, X., LOHSE, D., STEVENS, R.J.A.M. & VERZICCO, R. 2012*a* Logarithmic temperature profiles in turbulent Rayleigh–Bénard convection. *Phys. Rev. Lett.* **109**, 114501.

AHLERS, G., BODENSCHATZ, E., HARTMANN, R., HE, X., LOHSE, D., REITER, P., STEVENS, R.J.A.M., VERZICCO, R., WEDI, M. & WEISS, S. 2022 Aspect ratio dependence of heat transfer in a cylindrical Rayleigh–Bénard cell. *Phys. Rev. Lett.* **128**, 084501.

AHLERS, G., BODENSCHATZ, E. & HE, X. 2014 Logarithmic temperature profiles of turbulent Rayleigh–Bénard convection in the classical and ultimate state for a Prandtl number of 0.8. *J. Fluid Mech.* **758**, 436–467.

AHLERS, G., GROSSMANN, S. & LOHSE, D. 2009 Heat transfer and large scale dynamics in turbulent Rayleigh–Bénard convection. *Rev. Mod. Phys.* **81**, 503–537.

AHLERS, G., HE, X., FUNFSCHILLING, D. & BODENSCHATZ, E. 2012*b* Heat transport by turbulent Rayleigh–Bénard convection for $Pr \simeq 0.8$ and $3 \times 10^{12} \lesssim Ra \lesssim 10^{15}$: aspect ratio $\Gamma = 0.50$. *New J. Phys.* **14**, 103012.

BAO, Y., CHEN, J., LIU, B.F., SHE, Z.S., ZHANG, J. & ZHOU, Q. 2015 Enhanced heat transport in partitioned thermal convection. *J. Fluid Mech.* **784**, R5.

CECCIO, S.L. 2010 Friction drag reduction of external flows with bubble and gas injection. *Annu. Rev. Fluid Mech.* **42**, 183–203.

CHEN, J., BAO, Y., YIN, Z.X. & SHE, Z.S. 2017 Theoretical and numerical study of enhanced heat transfer in partitioned thermal convection. *Intl J. Heat Mass Transfer* **115**, 556–569.

CHING, E.S.C., DUNG, O.Y. & SHISHKINA, O. 2017 Fluctuating thermal boundary layers and heat transfer in turbulent Rayleigh–Bénard convection. *J. Stat. Phys.* **167**, 626–635.

CHING, E.S.C., LEUNG, H.S., ZWIRNER, L. & SHISHKINA, O. 2019 Velocity and thermal boundary layer equations for turbulent Rayleigh–Bénard convection. *Phys. Rev. Res.* **1**, 033037.

CHOI, C.H. & KIM, C.J. 2006 Large slip of aqueous liquid flow over a nanoengineered superhydrophobic surface. *Phys. Rev. Lett.* **96**, 066001.

DAVIS, R.E. 1991 Lagrangian ocean studies. *Annu. Rev. Fluid Mech.* **23**, 43–64.

GOLUSKIN, D. 2015 Internally heated convection beneath a poor conductor. *J. Fluid Mech.* **771**, 36–56.

GOLUSKIN, D., JOHNSTON, H., FLIERL, G.R. & SPIEGEL, E.A. 2014 Convectively driven shear and decreased heat flux. *J. Fluid Mech.* **759**, 360–385.

GROSSMANN, S. & LOHSE, D. 2000 Scaling in thermal convection: a unifying view. *J. Fluid Mech.* **407**, 27–56.

GROSSMANN, S. & LOHSE, D. 2001 Thermal convection for large Prandtl number. *Phys. Rev. Lett.* **86**, 3316–3319.

GROSSMANN, S. & LOHSE, D. 2011 Multiple scaling in the ultimate regime of thermal convection. *Phys. Fluids* **23**, 045108.

HE, X., BODENSCHATZ, E. & AHLERS, G. 2020*a* Absence of evidence for the ultimate state of turbulent Rayleigh–Bénard convection reply. *Phys. Rev. Lett.* **124**, 229402.

HE, X., BODENSCHATZ, E. & AHLERS, G. 2020*b* Aspect ratio dependence of the ultimate-state transition in turbulent thermal convection. *Proc. Natl Acad. Sci. USA* **117**, 30022.

HE, X., BODENSCHATZ, E. & AHLERS, G. 2021*a* A model for universal spatial variations of temperature fluctuations in turbulent Rayleigh–Bénard convection. *Theor. Appl. Mech. Lett.* **11**, 1.

HE, X., BODENSCHATZ, E. & AHLERS, G. 2021*b* Universal scaling of temperature variance in Rayleigh–Bénard convection near the transition to the ultimate state. *J. Fluid Mech.* **931**, A7.

HE, X., FUNFSCHILLING, D., BODENSCHATZ, E. & AHLERS, G. 2012*a* Heat transport by turbulent Rayleigh–Bénard convection for $Pr \simeq 0.8$ and $4 \times 10^{11} \lesssim Ra \lesssim 2 \times 10^{14}$: ultimate-state transition for aspect ratio $\gamma = 1.00$. *New J. Phys.* **14**, 063030.

HE, X., FUNFSCHILLING, D., NOBACH, H., BODENSCHATZ, E. & AHLERS, G. 2012*b* Transition to the ultimate state of turbulent Rayleigh–Bénard convection. *Phys. Rev. Lett.* **108**, 024502.

HUANG, M. & HE, X. 2022 Heat transport in horizontally periodic and confined Rayleigh–Bénard convection with no-slip and free-slip plates. *Theor. Appl. Mech. Lett.* **12**, 100330.

IYER, K.P., SCHEEL, J.D., SCHUMACHER, J. & SREENIVASAN, K.R. 2020 Classical 1/3 scaling of convection holds up to $Ra = 10^{15}$. *Proc. Natl Acad. Sci. USA* **117**, 7594.

KACZOROWSKI, M., CHONG, K.L. & XIA, K.Q. 2014 Turbulent flow in the bulk of Rayleigh–Bénard convection: aspect-ratio dependence of the small-scale properties. *J. Fluid Mech.* **747**, 73–102.

KRAICHNAN, R.H. 1962 Turbulent thermal convection at arbitrary Prandtl number. *Phys. Fluids* **5**, 1374–1389.

LOHSE, D. & XIA, K.Q. 2010 Small-scale properties of turbulent Rayleigh–Bénard convection. *Annu. Rev. Fluid Mech.* **42**, 335–364.

MELLADO, J.P. 2012 Direct numerical simulation of free convection over a heated plate. *J. Fluid Mech.* **712**, 418–450.

MOORE, W.B. & WEBB, A.A.G. 2013 Heat-pipe Earth. *Nature* **501**, 501–505.

PANDEY, A. & VERMA, M.K. 2016 Scaling of large-scale quantities in Rayleigh–Bénard convection. *Phys. Fluids* **28**, 095105.

VAN DER POEL, E.P., OSTILLA, R., VERZICCO, R. & LOHSE, D. 2014 Effect of velocity boundary conditions on the heat transfer and flow topology in two-dimensional Rayleigh–Bénard convection. *Phys. Rev.* E **90**, 013017.

VAN DER POEL, E.P., OSTILLA-MÓNICO, R., VERZICCO, R., GROSSMANN, S. & LOHSE, D. 2015 Logarithmic mean temperature profiles and their connection to plume emissions in turbulent Rayleigh–Bénard convection. *Phys. Rev. Lett.* **115**, 154501.

VAN DER POEL, E.P., STEVENS, R.J.A.M. & LOHSE, D. 2013 Comparison between two-and three-dimensional Rayleigh–Bénard convection. *J. Fluid Mech.* **736**, 177–194.

VAN DER POEL, E.P., STEVENS, R.J.A.M., SUGIYAMA, K. & LOHSE, D. 2012 Flow states in two-dimensional Rayleigh–Bénard convection as a function of aspect-ratio and Rayleigh number. *Phys. Fluids* **24**, 085104.

SCHLICHTING, H. & GERSTEN, K. 2000 *Boundary Layer Theory*, 8th edn. Springer.

SHISHKINA, O., HORN, S., EMRAN, M.S. & CHING, E.S.C. 2017 Mean temperature profiles in turbulent thermal convection. *Phys. Rev. Fluids* **2**, 113502.

SHISHKINA, O., HORN, S., WAGNER, S. & CHING, E.S.C. 2015 Thermal boundary layer equation for turbulent Rayleigh–Bénard convection. *Phys. Rev. Lett.* **114**, 114302.

SHISHKINA, O., STEVENS, R.J.A.M., GROSSMANN, S. & LOHSE, D. 2010 Boundary layer structure in turbulent thermal convection and its consequences for the required numerical resolution. *New J. Phys.* **12**, 075022.

SHISHKINA, O., WEISS, S. & BODENSCHATZ, E. 2016 Conductive heat flux in measurements of the Nusselt number in turbulent Rayleigh–Bénard convection. *Phys. Rev. Fluids* **1**, 062301(R).

SHRAIMAN, B.I. & SIGGIA, E.D. 1990 Heat transport in high-Rayleigh number convection. *Phys. Rev.* A **42**, 3650–3653.

SPIEGEL, E.A. 1971 Convection in stars. *Annu. Rev. Astron. Astrophys.* **9**, 323–352.

STEVENS, R.J.A.M., VAN DER POEL, E.P., GROSSMANN, S. & LOHSE, D. 2013 The unifying theory of scaling in thermal convection: the updated prefactors. *J. Fluid Mech.* **730**, 295–308.

TRITTON, D.J. 1975 Internally heated convection in the atmosphere of Venus and in the laboratory. *Nature* **257**, 110–112.

VON HARDENBERG, J., GOLUSKIN, D., PROVENZALE, A. & SPIEGEL, E.A. 2015 Generation of large-scale winds in horizontally anisotropic convection. *Phys. Rev. Lett.* **115**, 134501.

WANG, Q., CHONG, K.L., STEVENS, R.J.A.M., VERZICCO, R. & LOHSE, D. 2020*a* From zonal flow to convection rolls in Rayleigh–Bénard convection with free-slip plates. *J. Fluid Mech.* **905**, A21.

WANG, Q., LOHSE, D. & SHISHKINA, O. 2021 Scaling in internally heated convection: a unifying theory. *Geophys. Res. Lett.* **48**, e2020GL091198.

WANG, Q., VERZICCO, R., LOHSE, D. & SHISHKINA, O. 2020*b* Multiple states in turbulent large-aspect-ratio thermal convection: what determines the number of convection rolls? *Phys. Rev. Lett.* **125**, 074501.

WANG, Y., HE, X. & TONG, P. 2016 Boundary layer fluctuations and their effects on mean and variance temperature profiles in turbulent Rayleigh–Bénard convection. *Phys. Rev. Fluids* **1**, 082301(R).

WANG, Y., XU, W., HE, X., YIK, H., WANG, X., SCHUMACHER, J. & TONG, P. 2018 Boundary layer fluctuations in turbulent Rayleigh–Bénard convection. *J. Fluid Mech.* **840**, 408–431.

WEISS, S. & AHLERS, G. 2011 Turbulent Rayleigh–Bénard convection in a cylindrical container with aspect ratio $\Gamma = 0.50$ and Prandtl number $Pr = 4.38$. *J. Fluid Mech.* **676**, 5–40.

WEISS, S. & AHLERS, G. 2013 Effect of tilting on turbulent convection: cylindrical samples with aspect ratio $\Gamma = 0.50$. *J. Fluid Mech.* **715**, 314–334.

WEISS, S., HE, X., AHLERS, G., BODENSCHATZ, E. & SHISHKINA, O. 2018 Bulk temperature and heat transport in turbulent Rayleigh–Bénard convection of fluids with temperature-dependent properties. *J. Fluid Mech.* **851**, 374–390.

WEN, B., GOLUSKIN, D., LEDUC, M., CHINI, G.P. & DOERING, C.R. 2020 Steady Rayleigh–Bénard convection between stress-free boundaries. *J. Fluid Mech.* **905**, R4.

WHITE, C.M. & MUNGAL, M.G. 2008 Mechanics and prediction of turbulent drag reduction with polymer additives. *Annu. Rev. Fluid Mech.* **40**, 235–56.

XI, H.D. & XIA, K.Q. 2008 Flow mode transition in turbulent thermal convection. *Phys. Fluids* **20**, 055104.

XU, W., WANG, Y., HE, X., WANG, X., SCHUMACHER, J., HUANG, S. & TONG, P. 2021 Mean velocity and temperature profiles in turbulent Rayleight–Bénard convection at low Prandtl numbers. *J. Fluid Mech.* **918**, A1.

YAN, B., SHISHKINA, O. & HE, X. 2021 Thermal boundary-layer structure in laminar horizontal convection. *J. Fluid Mech.* **915**, R5.

ZHANG, Y.Z., SUN, C., BAO, Y. & ZHOU, Q. 2018 How surface roughness reduces heat transport for small roughness heights in turbulent Rayleigh–Bénard convection. *J. Fluid Mech.* **836**, R2.

ZWIRNER, L. & SHISHKINA, O. 2018 Confined inclined thermal convection in low-Prandtl-number fluids. *J. Fluid Mech.* **850**, 984–1008.

ZWIRNER, L., TILGNER, A. & SHISHKINA, O. 2020 Elliptical instability and multi-roll flow modes of the large-scale circulation in confined turbulent Rayleigh–Bénard convection. *Phys. Rev. Lett.* **125**, 054502.